International Journal of Scientific Research in Science and Technology
Available online at : www.ijsrst.com
OPEN ACCESS
Print ISSN: 2395-6011 | Online ISSN: 2395-602X
doi : https://doi.org/10.32628/IJSRST

Fe_2O_3–g-C_3N_4 Nanocomposites for Photocatalysis: A Comprehensive Review on Synthetic Approaches, Characterization Techniques, Mechanistic Insights, and Environmental Applications

Babasaheb T. Shinde[1,2], Hemant V. Chavan[1*]
[1]Department of Chemistry, A.S.P. College (Autonomous), Devrukh, Dist. Ratnagiri-415 804, Maharashtra. India
[2]Department of Chemistry, S.K.S.V. College, Lanja, Dist. Ratnagiri-, Maharashtra. India

ARTICLEINFO

Article History:
Published : 30 April 2025

Publication Issue :
Volume 12, Issue 13
March-April-2025

Page Number :
243-268

ABSTRACT

This review compiles and critically analyses recent developments in the synthesis, characterisation, and photocatalytic applications of g-C_3N_4-Fe2O3 nanocomposites. As a promising class of heterostructure materials, these composites integrate the visible-light activity of graphitic carbon nitride (g-C_3N_4) with the redox-active, magnetically separable iron oxide (Fe_2O_3) to improve photocatalytic degradation of organic pollutants. the present study emphasises the influence of various synthesis approaches, ranging from conventional chemical methods to eco-friendly strategies involving plant extracts, industrial waste, and laterite soil, on the materials' structural properties as well as their functional performance. Particular focus is placed on the formation of heterojunctions and their pivotal role in promoting efficient charge separation. Based on recent studies, supported by band structure analysis and spectroscopic evidence, the mechanistic pathways, such as Type II, Z-scheme and S-scheme, are thoroughly examined. Although these nanocomposites demonstrate >90% degradation efficiency for various dyes, long-term stability, environmental impact, and large-scale production remain. This article aims to provide a comprehensive understanding of the current state of research on g-C_3N_4-Fe_2O_3 nanocomposites and their potential for sustainable photocatalytic applications.

Keywords: Iron oxide nanoparticles, Graphitic carbon nitride, Photocatalysis, Nanocomposites, Wastewater treatment.

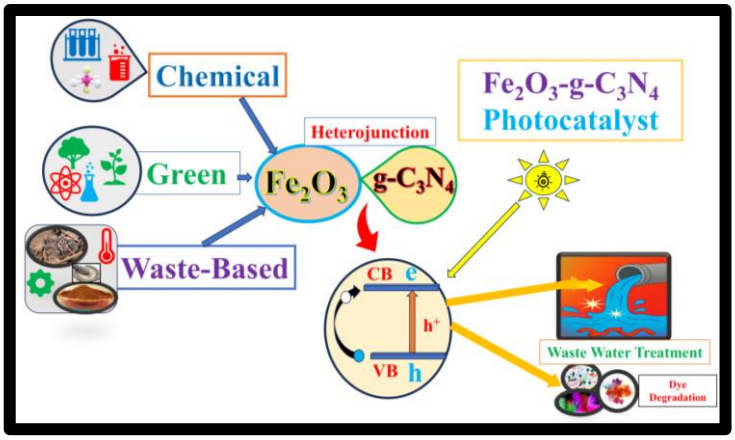

Fig.1. Graphical Abstract

INTRODUCTION

1.1 Environmental Challenges and the Rise of Photocatalytic Solutions

In recent years, extensive research has highlighted the growing burden of water pollution caused by industrial dyes, pharmaceuticals, pesticides, and other persistent organic pollutants (POPs)[1]. Conventional wastewater treatment technologies, although widely used, are often insufficient to address these complex contaminants due to limitations in efficiency, selectivity, and sustainability[2].Photocatalysis has been extensively explored in the literature as a sustainable and green approach for degrading hazardous pollutants in wastewater[3]. Unlike physical or biological treatment methods, photocatalysis enables direct mineralization of pollutants using light energy, without generating harmful byproducts[4].

Iron oxide (Fe_2O_3) and graphitic carbon nitride (g-C_3N_4) have been extensively studied asphotocatalysts due to their distinct properties[5]. Fe_2O_3 offers narrow band gap energy (~2.1 eV), magnetic separability, chemical stability, and earth abundance, making it cost-effective and environmentally benign[6]. On the other hand, g-C_3N_4 is a visible-light-active, metal-free polymeric semiconductor with a moderate band gap (~2.7 eV), good thermal stability, and facile synthesis from inexpensive precursors like urea or melamine[7]. Numerous studies have reported that their individual photocatalytic performance is limited by the rapid recombination of photogenerated charge carriers. However, their integration into a heterojunction system can mitigate these limitations, which justifies the growing interest in these materials as components of nanocomposite photocatalysts[8].

Recent literature highlights the strategic use of various dopants and modifiers to enhance the photocatalytic performance of Fe_2O_3-based systems. Carbonaceous materials such as graphene, reduced graphene oxide (rGO), and graphene oxide (GO) have been frequently employed to improve electrical conductivity and facilitate charge carrier mobility, thereby suppressing electron–hole recombination. Metal oxide dopants like TiO_2 and ZnO are valued for their oxidative strength and photostability, although their photocatalytic activity is typically confined to the UV region due to wide band gaps. To extend their response into the visible range, these oxides are often combined with Fe_2O_3 in heterostructured systems. Other modifiers, including SnO_2, carbon nanotubes (CNTs), Ag/AgCl, and biochar, contribute to enhanced surface area, improved charge separation, and localized surface plasmon resonance (LSPR) effects. Such modifications significantly improve light-harvesting capability, charge transfer efficiency, and overall degradation performance of Fe_2O_3

composites. Nevertheless, achieving optimal photocatalytic efficiency often requires rational design and synergistic integration within a multi-component nanocomposite framework, as outlined in **Table 1**.

Table 1. Comparative analysis of Fe_2O_3 composite materials based on structural features, photocatalytic performance, and electronic properties

Composite Material	Type	Typical Band Gap (eV)	Key Advantages in Composites	Limitations	References
g-C_3N_4	Polymeric semiconductor	~2.7	Visible light response, suitable band alignment with Fe_2O_3, thermal stability, metal-free	Low surface area, fast charge recombination	[9], [10]
Graphene	2D Carbon (semimetal)	~0	High conductivity, large surface area, fast electron transfer	No band gap (not ideal alone in photocatalysis), requires hybridization	[11], [12]
GO	Oxidized Graphene	~2.2–3.5	Tunable band gap, surface functional groups aid dispersion	Poor conductivity, unstable under light	[13], [14]
rGO	Partially reduced GO	~0.5–1.5	Better conductivity than GO, facilitates charge transfer	Residual oxygen can limit performance, structural defects	[15], [16]
TiO_2	Metal oxide semiconductor	~3.2 (anatase)	High stability, strong oxidizing ability	UV-active only, wide band gap limits solar efficiency	[17]
ZnO	Metal oxide semiconductor	~3.2	High exciton binding energy, easy synthesis	Photocorrosion, UV-active	[18]
SnO_2	Metal oxide semiconductor	~3.6	High mobility, good optical transparency	Limited visible light absorption	[19]
CNTs	Carbon-based nanostructure	~0–1	High conductivity, strong mechanical properties	Poor light absorption unless hybridized	[20]
Ag/AgCl	Plasmonic composite	~3.25 (AgCl)	Plasmon-enhanced visible absorption, strong oxidation	Stability issues under light, cost	[21]
Biochar	Carbon-rich porous material	Variable	Low cost, high surface area, eco-friendly	Low conductivity, limited electronic interaction	[22], [23]

The formation of Fe_2O_3/g-C_3N_4 nanocomposites is motivated by the need to overcome each material's intrinsic drawbacks and exploit synergistic interactions for enhanced photocatalytic performance. Reviewed studies consistently report that coupling these semiconductors leads to improved charge carrier separation, broader light absorption, and higher reactive oxygen species (ROS) generation. The heterojunction interfacewhether

traditional, Z-scheme, or S-scheme is crucial in driving efficient charge dynamics. Moreover, the magnetic property of Fe_2O_3 facilitates catalyst recovery, while g-C_3N_4 enhances surface area and dye adsorption. Together, they create a platform that addresses key challenges in environmental photocatalysis, particularly in degrading resistant organic dyes under visible or solar light[24].

This review aims to provide a thorough overview of recent studies on the synthesis of iron oxide (Fe_2O_3) nanoparticles derived from low-cost, abundant, and sustainable sources, including industrial waste, laterite soil, and plant extracts as well as some biogenic methods with a specific emphasis on their combining with graphitic carbon nitride (g-C_3N_4) to generate multifunctional nanocomposites. It also discusses characterization techniques essential for a detailed understanding of the structural, morphological, compositional, optical, magnetic, and surface properties of Fe_2O_3 nanocomposites, which directly influence their performance in catalyticapplications. Particular focus is directed on comprehending the improved photocatalytic performance of Fe_2O_3/g-C_3N_4 nanocomposites under UV-visible and sunlight exposure, also clarified through heterojunction mechanisms like Type II, Z-scheme, and S-scheme. This review also highlights the environmental applications of Fe_2O_3-g-C_3N_4 nanocomposites, thus providing future guidance for the strategic development of sustainable, high-performance nanocomposite catalysts (Fig. 1).

Synthesis Methods of Iron Oxide (Fe_2O_3) Nanoparticles

The synthesis of Fe_2O_3 nanoparticles from sustainable sources involves a broad spectrum of techniques. These methods can be broadly categorized into chemical, green/biological, and physical approaches. Each synthesis pathway offers unique scalability, morphology control, environmental impact, and application specificity advantages (**Fig. 2**).

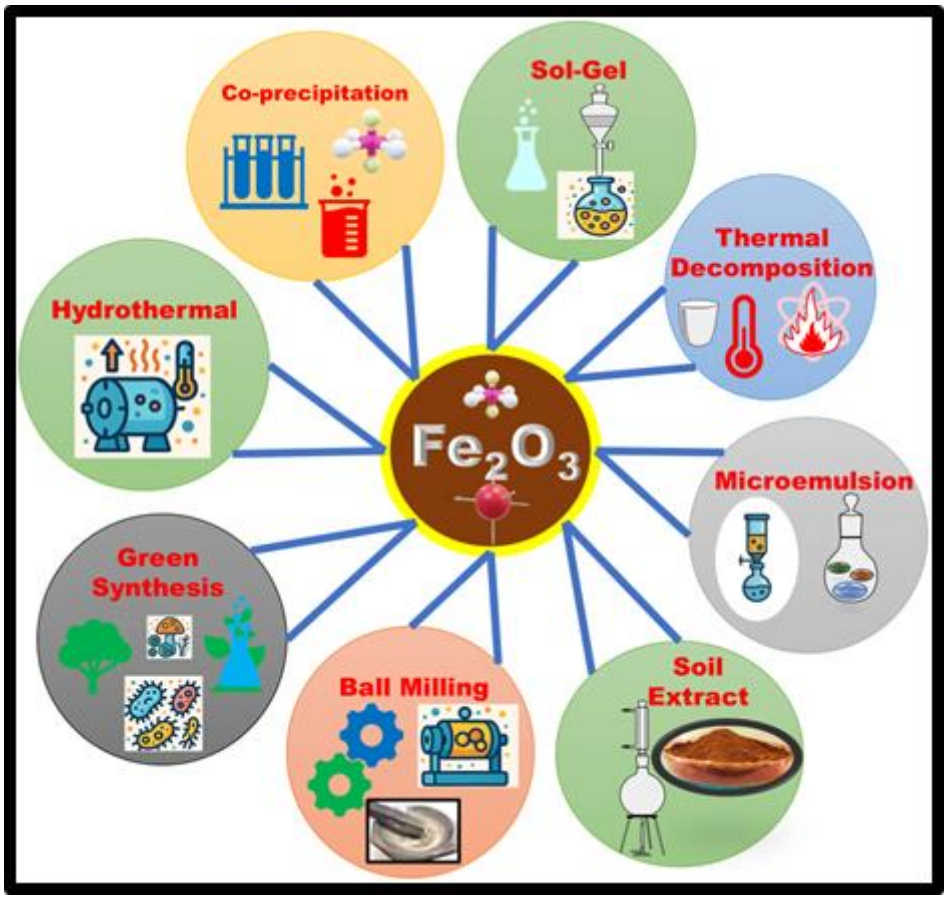

Fig.2 Various Synthetic Methods

2.1 Chemical Synthesis Methods

2.1.1 Co-precipitation Method:

The co-precipitation technique is one of the most efficient and widely used methods for synthesising iron oxide nanoparticles. It involves the simultaneous precipitation of Fe^{2+} and Fe^{3+} salts by adding a base such as NaOH or NH_4OH under controlled pH (typically around 9–11) and temperature conditions. The reaction leads to forming iron hydroxide precursors, which are then subjected to filtration, washing, and drying. Subsequent calcination at elevated temperatures enhances crystallinity, removes residual organics, and ensures phase purity, yielding well-defined Fe_2O_3 nanoparticles. This method is cost-effective, scalable, and suitable for chemical and green synthesis routes.

2.1.2 Sol-Gel Method

The sol-gel process involves the hydrolysis and polycondensation of iron precursors such as iron alkoxides or salts to form a colloidal suspension, which gradually evolves into a three-dimensional gel network. This gel is then aged, dried to remove solvents, and calcined at elevated temperatures to produce Fe_2O_3 nanoparticles. The method allows excellent control over composition, particle size, and morphology. It yields highly uniform, porous, and thermally stable nanoparticles, making it suitable for catalytic and electronic applications.

2.1.3 Hydrothermal/Solvothermal Method:

This method involves the crystallization of iron precursors in sealed autoclaves at elevated temperatures (typically 120–200°C) using water (hydrothermal) or organic solvents (solvothermal) as reaction media. The high-pressure environment promotes the formation of highly crystalline Fe_2O_3 nanoparticles with controlled size, morphology, and phase. Various nanostructures like rods, sheets, spheres, and cubes can be synthesized by tuning parameters such as temperature, time, pH, and solvent type. This method is especially advantageous for producing uniform, monodispersed particles with enhanced surface properties.

2.1.4 Thermal Decomposition:

This technique involves the thermal analysis of iron-based organometallic precursors in organic solvents, typically in the presence of surfactants or stabilizing agents. These surfactants help control nanoparticle growth, prevent aggregation, and enable the formation of highly monodisperse Fe_2O_3 nanoparticles. The method yields uniform particles with excellent crystallinity and allows fine control over size and morphology, making it suitable for biomedical and electronic applications.

2.1.5 Microemulsion and Reverse Micelle Techniques:

These methods use thermodynamically stable, surfactant-stabilized nanoscale emulsions (microemulsions) as nanoreactors for the controlled synthesis of Fe_2O_3 nanoparticles. In reverse micelles, water droplets dispersed in an organic solvent act as confined reaction zones where nucleation and growth occur, offering precise control over particle size and distribution. The approach enables the synthesis of ultra-small, monodisperse nanoparticles with uniform morphology. Despite being limited by low yield and complex separation, these techniques are valuable for fundamental studies and applications requiring high uniformity.

2.2 Green Synthesis (Eco-friendly/Biogenic Routes)

2.2.1 Plant Extract Mediated Synthesis:

This green synthesis approach employs bioactive compounds such as flavonoids, polyphenols, alkaloids, and proteins in plant extracts as natural reducing and stabilizing agents. Iron salts are typically reacted with the extract at room or mildly elevated temperatures, leading to the formation of Fe_2O_3 nanoparticles under eco-friendly conditions. The method is cost-effective and sustainable, avoiding toxic chemicals, aligning with green chemistry principles. It also offers tunable morphology and functional properties depending on the phytochemical composition of the extract.

2.2.2 Bacteria, Fungi, and Algae Mediated Synthesis:

In this biogenic approach, microorganisms like bacteria, fungi, and algae facilitate the reduction of iron ions into Fe_2O_3 nanoparticles through enzymatic and metabolic pathways. These microbes secrete enzymes, proteins, and other biomolecules that act as natural reducing and capping agents. The synthesis can occur intracellularly or extracellularly, depending on the organism and conditions. Although this method is eco-friendly and yields stable nanoparticles, it demands sterile environments, careful culture maintenance, and longer reaction times.

2.2.3 Soil and Mineral Source Extraction:

This method uses naturally abundant, iron-rich sources such as laterite or red soil for the synthesis of Fe_2O_3 nanoparticles. The process typically involves acid leaching to extract iron ions, followed by controlled precipitation using a base and subsequent calcination to obtain crystalline nanoparticles. It offers a sustainable and low-cost route by converting natural or waste materials into valuable nanomaterials. The approach aligns well with circular economy principles and is suitable for large-scale, eco-friendly applications.

2.2.4 Biowaste-Derived Synthesis:

This eco-friendly approach involves using iron-containing biowaste materials such as rusty iron tools, iron slag, or plant ashes as precursors for synthesizing Fe_2O_3 nanoparticles. The iron is typically extracted through acid or base treatment, followed by precipitation and calcination steps. This method promotes waste valorisation, reduces environmental burden, and supports sustainable nanomaterial production. It also aligns with green chemistry and circular economy frameworks, offering a low-cost and scalable synthesis route.

2.3 Physical Methods

2.3.1 High-Energy Ball Milling

High-energy ball milling is a top-down approach that involves the mechanical grinding of iron-containing materials, such as iron powders or ores, in a high-energy ball mill. The repeated collisions of grinding media break the bulk material into smaller particles, facilitating the formation of nanostructures. This method enables precise particle size and morphology control, producing highly dispersed Fe_2O_3 nanoparticles. It is particularly advantageous for fabricating nanoparticles with uniform size distributions, although it may require post-milling treatment to remove surface defects and improve crystallinity.

The comprehensive overview of the synthetic methods for Fe2O3 nanoparticles is given in Table 2.

Table 2. Comparative Overview of Synthesis Techniques and Methods

Method	Precursor	Conditions	Advantages	Limitations	Ref.
Co-precipitation	(Ferric nitrate and Oxalic acid	water as a solvent, 250-450°C	High surface area, porous structure	Requires calcination,	[25]
Sol–gel	$Fe(NO_3)_3 \cdot 9H_2O$, Epoxypropane	Hydrolysis in non-aqueous solvent; supercritical CO_2 drying; calcination <300°C.	High surface area; good pore structure; environmentally friendly reagents.	Complex setup for supercritical fluid process; high cost of equipment.	[26]
Hydrothermal	$FeCl_3 \cdot 6H_2O$	Solvent variation (water/ethanol), 160–180°C, 6–24 hours.	Morphology control (nanoplates, nanorods); no surfactants required.	Agglomeration risks; require precise solvent control.	[27]

Method	Precursor	Conditions	Advantages	Limitations	Ref.
Thermal Decomposition	Iron acetate ($Fe(CH_3COO)_3$	Heated to 400°C in air; followed by annealing for mesoporous structure.	Produces mesoporous α-Fe_2O_3 films directly on substrates; scalable for large-area applications.	Requires post-synthesis annealing for pore formation and crystallinity.	[28]
Microemulsion	$FeCl_3 \cdot 6H_2O$, NaOH	n-heptane as oil phase, AOT as surfactant, 1-butanol as co-surfactant; calcination at 500°C.	Produces plate-like α-Fe_2O_3 nanoparticles (~13.1 nm); homogeneous dispersion; optical band gap ~3.2 eV.	Requires calcination; surfactant removal necessary; limited scalability.	[29]
Plant Extract (Green)	$FeCl_3 \cdot 6H_2O$	Methanol extract mixed with $FeCl_3$ solution; heated at 80°C for 2 hours.	Rapid heating profile for hyperthermia applications; SAR values ~62.75 W/g at low NP concentration.	Requires methanol extraction and sodium acetate addition; limited scalability for larger volumes.	[30]
Bacterial/Fungal	$FeSO_4$	Incubation with Bacillus sp. GMS10 at 37°C for 24–36 hours under aerobic conditions.	Eco-friendly, low-cost, and scalable; produces α-Fe_2O_3 nanoparticles (~30 nm) with antibacterial and anti-biofilm properties.	Requires precise bacterial culture conditions; potential contamination risks.	[31]
Laterite soil extraction	Acid-treated laterite	5M HCl + 650°C calcine	Abundant source, waste valorization	Purity and reproducibility issues	[32]
Biowaste/rust	Scrap iron, rust	Rust dissolved in HCl, followed by precipitation with NaOH; dried at 110°C.	Simple and scalable; converts waste rust into α-Fe_2O_3 nanoparticles (~20–50 nm).	Requires acid treatment; potential environmental concerns with acid disposal.	[33]
Ball Milling	Fe_2O_3 powder	Milling at 300–600 rpm for 5–10 hours under inert atmosphere; sintering at 600–800°C.	Produces nanoscale Fe_2O_3 with lattice distortion; improves mechanical and magnetic properties.	Requires high-energy equipment; risk of contamination from milling media.	[34]

A comprehensive table of data on synthetic methodologieshas been developed for the preparation of Fe_2O_3 nanoparticles, each method offering unique significance in terms of morphology, surface area, and functional applicability. Conventional chemical routes such as co-precipitation, sol–gel, and hydrothermal synthesis provide reasonable control over particle characteristics but often require high-temperature treatments or complex setups. Green and biogenic approaches, including plant extract and microbial-assisted synthesis, present environmentally friendly and scalable alternatives with added biological functionalities. Waste-derived methods utilizing laterite, rust, or industrial by-products offer sustainable, cost-effective routes aligned with circular economy goals. Ultimately, the choice of synthesis method should be guided by the desired application, scalability, cost, and environmental impact.

Characterisation Techniques and Their Importance

There are various characterization techniques in confirming the synthesis, structural integrity, and functional properties of Fe_2O_3, g-C_3N_4, and their g–C_3N_4–Fe_2O_3 nanocomposites. These techniques are essential for understanding the materials' phase, morphology, optical properties, surface characteristics, magnetic behaviour, and thermal stability, directly influencing their photocatalytic degradation performance. A detailed discussion of each technique will follow in the next section.

3.1 X-ray Diffraction (XRD)

The X-ray diffraction (XRD) analysis of the synthesized materials provides clear evidence of their crystallinity and phase identification. For Fe_2O_3, the presence of well-defined peaks at 24.2°, 33.1°, and 35.5° corresponding to the (110), (113), and (024) diffraction planes confirms the formation of hematite (α-Fe_2O_3), indicating a highly crystalline structure[35]. Similarly, the g-C_3N_4 material shows characteristic peaks at 12.15° and 27.4° corresponding to the (100) and (002) planes, confirming the successful synthesis of graphitic carbon nitride[36]. In the case of the g-C_3N_4-Fe_2O_3 composite, the XRD pattern exhibits a combination of peaks from both Fe_2O_3 (at 24.2°) and g-C_3N_4 (at 13.0° and 27.4°), indicating the successful formation of the composite material[37]. The observed overlapping peaks suggest that the two components have been effectively integrated, maintaining their individual crystal structures, and confirming the synthesis of a composite material with distinct phases of Fe_2O_3 and g-C_3N_4 a Table 3. Highlighted various Phases, Peak position and its diffraction planes.

Table 3. XRD data of g-C_3N_4, Fe_2O_3 and g-C_3N_4-Fe_2O_3 nanocomposite

Material	Phase Identified	Peak Position (2θ)	Corresponding Diffraction Planes	Remarks
Fe_2O_3	Hematite (α-Fe_2O_3)	24.2°, 33.1°, 35.5°	(110), (113), (024)	Well-defined peaks confirming crystallinity
g-C_3N_4	Graphitic Carbon Nitride	13.0°, 27.4°	(100), (002)	Characteristic peaks for g-C_3N_4 structure
g-C_3N_4–Fe_2O_3 Composite	Mixture of Hematite and g-C_3N_4	13.0°, 24.2°, 27.4°	(100), (110), (002), (113)	Composite shows combined peaks of Fe_2O_3 and g-C_3N_4, indicating successful synthesis

3.2 Fourier Transform Infrared Spectroscopy (FTIR)

The FT-IR spectra of Fe_2O_3, g-C_3N_4, and their composite (g-C_3N_4-Fe_2O_3) reveal characteristic functional group vibrations that confirm the formation of each material and their composite. For Fe_2O_3, prominent peaks at ~3430 cm^{-1} and ~1620 cm^{-1} correspond to O-H stretching and bending vibrations, while a peak at ~530 cm^{-1} indicates Fe-O stretching, characteristic of hematite[38]. In g-C_3N_4, the key peaks at ~3115 cm^{-1} and ~1600 cm^{-1} are attributed to N-H stretching and C=N stretching, respectively, while the peaks at ~1200 cm^{-1} and ~800 cm^{-1} correspond to C-N stretching and C–C bending, confirming the presence of the triazine ring structure[39]. In the g-C_3N_4/Fe_2O_3 composite, the FT-IR spectrum shows a combination of peaks from both Fe_2O_3 and g-C_3N_4, including O-H and C-N stretching vibrations, alongside the Fe-O stretching vibration, indicating successful incorporation of both components into a composite material. These FT-IR results validate the successful synthesis of the g-C_3N_4/Fe_2O_3 nanocomposite with distinct phases[40]. Table 4. Listed various peaks and vibration modes of FT-IR peaks of g-C_3N_4, Fe_2O_3, and g-C_3N_4-Fe_2O_3 nanocomposite

Table 4.FT-IR data of g-C_3N_4, Fe_2O_3 and g-C_3N_4-Fe_2O_3 nanocomposite

Material	FT-IR Peaks (cm^{-1})	Vibration Mode	Remarks
Fe_2O_3	3430, 1620, 530	O-H stretching, O-H bending, Fe-O stretching	Characteristic peaks for the Fe_2O_3 structure
g-C_3N_4	3115, 1600, 1200, 800	N-H stretching, C=N stretching, C-N stretching, C–C bending	Characteristic peaks for graphitic carbon nitride
g-C_3N_4–Fe_2O_3 Composite	3430, 1620, 1600, 530, 1200	O-H stretching, O-H bending, C=N stretching, Fe-O stretching, C-N stretching	Peaks from both Fe_2O_3 and g-C_3N_4 indicate successful composite formation

3.3 Uv-Vis Diffuse Reflectance Spectroscopy (DRS)

UV-Vis Diffuse Reflectance Spectroscopy (DRS) is a crucial technique to evaluate semiconductor photocatalysts' optical properties and bandgap energies. Fe_2O_3 shows strong absorption in the visible region with an absorption edge around 520–580 nm and a bandgap of approximately 2.0–2.2 eV. However, its photocatalytic performance is limited by rapid electron–hole recombination. In contrast, g-C_3N_4 exhibits a slightly higher bandgap (~2.6–2.8 eV) and absorbs up to 460 nm, offering good stability but restricted activity due to low surface area and fast charge recombination[41]. The formation of a g–C_3N_4-Fe_2O_3nanocomposite leads to a redshift in the absorption edge (~540–580 nm) and a reduced bandgap (~1.9–2.2 ev), indicating improved visible-light absorption. This enhancement is attributed to forming Z-scheme or S-scheme heterojunctions, which promote efficient charge carrier separation and suppress recombination, making the composite a promising material for photocatalytic applications[42].Table 5highlights various peaks, band gap, and nature of transition of UV-Vis DRS peaks of g-C_3N_4, Fe_2O_3, and g-C_3N_4-Fe_2O_3 nanocomposite.

Table 5. UV-Vis DRS peaks of g-C_3N_4, Fe_2O_3, and g-C_3N_4-Fe_2O_3 nanocomposite

Material	Absorption Edge (nm)	Bandgap (eV)	Nature of Transition	Critical Remarks
Fe_2O_3	~520–580	2.0–2.2	Indirect (d–d)	- Strong visible-light absorption capability.

Material	Absorption Edge (nm)	Bandgap (eV)	Nature of Transition	Critical Remarks
				- Suffers from rapid electron–hole recombination. - Limited photocatalytic efficiency when used alone.
g-C_3N_4	~440–460	2.6–2.8	Direct (n–π*)	- Good thermal and chemical stability. - Absorbs visible light up to ~460 nm. - Low surface area and fast recombination restrict activity.
g-C_3N_4–Fe_2O_3	~540–580	1.9–2.2	Mixed (Z-/S-scheme)	- Redshift in absorption edge enhances light utilization. - Heterojunction formation improves charge separation. - Suitable for Z-/S-scheme photocatalytic applications.

3.4 X-ray Photoelectron Spectroscopy (XPS)

XPS spectraprovide essential insights into the elemental composition, chemical states, and interfacial interactions within nanocomposites (**Table 6.**). In the case of Fe_2O_3, characteristic Fe 2p peaks at ~710.8 eV (Fe $2p_{3/2}$) and ~724.5 eV (Fe $2p_{1/2}$), along with a satellite peak near 719 eV, confirm the Fe^{3+} oxidation state typical of α-Fe_2O_3[43]. For g-C_3N_4, the presence of C 1s peaks at ~284.6 eV (C–C) and ~288.2 eV (N–C=N), and N 1s peaks around 398.6 eV and 400.1 eV, indicates the dominance of sp^2-hybridized C–N frameworks and bridging nitrogen atoms within triazine or heptazine units. Upon composite formation (g–C_3N_4–Fe_2O_3), notable shifts in the binding energies of N 1s and C 1s spectra and the consistent presence of Fe^{3+} peaks suggest strong electronic interaction at the heterojunction interface[44]. These shifts indicate chemical bonding, likely through Fe–N or Fe–O–C linkages, which enhance charge transfer and contribute to the improved photocatalytic performance of the composite system[45].

Table 6. XPS peaks and binding energy of g-C_3N_4, Fe_2O_3, and g-C_3N_4-Fe_2O_3 nanocomposite

Material	Key Binding Energies (eV)	Observed Elements & States	Critical Remarks
Fe_2O_3	Fe $2p_{3/2}$: ~710.8 eV Fe $2p_{1/2}$: ~724.5 eV Satellite: ~719 eV	Fe^{3+} oxidation state confirmed Presence of satellite peak supports α-Fe_2O_3	- Fe^{3+} state confirms hematite phase. - Strong satellite peak indicates good crystallinity. - No significant Fe^{2+} detected.
g-C_3N_4	C 1s: ~284.6 eV (C–C), ~288.2 eV (N–C=N) N 1s: ~398.6 eV (C–N=C), ~400.1 eV (N–$(C)_3$)	sp^2 C–N frameworks and bridging nitrogen species	- Peak positions confirm triazine/heptazine units. - High N/C ratio indicates polymeric structure. - Minor C–C peak may arise from adventitious carbon.

Material	Key Binding Energies (eV)	Observed Elements & States	Critical Remarks
g-C_3N_4–Fe_2O_3	Fe 2p similar to Fe_2O_3 N 1s: slight shift to lower BE C 1s: shift in N–C=N	Coexistence of Fe^{3+}, C–N, and N–Fe interactions	- Binding energy shifts suggest chemical interaction at interface. - Presence of Fe–N bonding confirms strong coupling. - Synergistic electronic structure favors charge transfer.

3.5 Field Emission Scanning Electron Microscopy (FE-SEM)

SEM provides high-resolution images of surface morphology and the distribution of Fe_2O_3 and g-C_3N_4 within composites**(Table 7).** It is essential for visualizing particle size, shape, and the homogeneity of the composite. The FE-SEM analysis reveals that Fe_2O_3 nanoparticles show agglomerated spherical morphology (~30–80 nm), while g-C_3N_4 displays layered, sheet-like structures. In the g–C_3N_4–Fe_2O_3 composite, Fe_2O_3 particles are uniformly dispersed over the g-C_3N_4 sheets, improving interfacial contact and reducing agglomeration. This morphology enhances surface area and facilitates better charge separation, supporting superior photocatalytic activity[46].

Table 7. SEM images and Morphology of g-C_3N_4, Fe_2O_3, and g-C_3N_4-Fe_2O_3 nanocomposite

Material	Observed Morphology	Particle Size / Shape	Critical Remarks
Fe_2O_3	Agglomerated, irregular spherical particles	~30–80 nm	- Shows uniform nanoscale grain formation. - Some degree of aggregation observed. - Porous texture beneficial for surface reactions.
g-C_3N_4	Layered, flaky sheet-like structure	Nanosheets or stacks	- Exhibits lamellar structure with wrinkled morphology. - High surface area but prone to stacking. - May limit photocatalytic efficiency due to low conductivity.
g-C_3N_4–Fe_2O_3	Fe_2O_3 particles dispersed over g-C_3N_4 sheets	Fe_2O_3 embedded in g-C_3N_4 matrix	- Uniform dispersion of Fe_2O_3 enhances active sites. - Improved interfacial contact supports charge transfer. - Reduced agglomeration and enhanced surface roughness aid catalysis.

3.6 High resolution-Transmission Electron Microscopy (HR-TEM)

HR-TEM used to analyse morphology and lattice spacing of material **(Table 8)** images show that Fe_2O_3 nanoparticles exhibit well-defined spherical morphology with sizes ranging from ~30 to 60 nm and distinct lattice fringes corresponding to the (104) plane. g-C_3N_4 appears as crumpled nanosheets with a thickness of ~3–5 nm, showing limited crystallinity at the edges. In the g-C_3N_4–Fe_2O_3 composite, Fe_2O_3 particles are uniformly

dispersed on the g-C_3N_4 sheets, with particle sizes around 20–40 nm and similar lattice spacing[47]. This uniform dispersion improves the composite's charge separation and photocatalytic efficiency by facilitating enhanced interfacial contact between the two phases[48].

Table 8. HR-TEM images and lattice space of g-C_3N_4, Fe_2O_3, and g-C_3N_4-Fe_2O_3 nanocomposite

Material	Morphology / Structure	Particle Size / Lattice Spacing	Critical Remarks
Fe_2O_3	Well-defined spherical particles	~30–60 nm, lattice spacing ~0.29 nm (101)	- High crystallinity with distinct lattice fringes. - Uniform nanoparticle size with good stability.
g-C_3N_4	Crumpled nanosheets, amorphous at edges	Nanosheet thickness ~3–5 nm	- Shows irregular sheet formation. - Limited crystallinity and higher porosity.
g-C_3N_4–Fe_2O_3	Fe_2O_3 particles dispersed on g-C_3N_4 sheets	Fe_2O_3 particles ~20–40 nm, lattice spacing ~0.29 nm (101)	- Fe_2O_3 uniformly dispersed over g-C_3N_4. - Enhanced interfacial contact facilitates efficient charge transfer.

3.7 Photoluminescence Spectroscopy (PL)

Photoluminescence (PL) Spectroscopy is another important tool used to study the significant differences in charge carrier dynamics across the materials**(Table 9).**Fe_2O_3 exhibits a broad emission band around 650–750 nm, indicative of high charge recombination rates, which hinder its photocatalytic performance. g-C_3N_4 shows a moderate PL intensity with emission peaks around 450–500 nm, suggesting a lower rate of charge recombination and better charge carrier retention, making it a promising photocatalyst. The g-C_3N_4-Fe_2O_3 composite demonstrates a redshifted emission peak (~550–600 nm) and a reduction in PL intensity, indicating enhanced charge separation and minimisedelectron-hole recombination, thus improving its photocatalytic efficiency[49].

Table 9. PL spectra of g-C_3N_4, Fe_2O_3, and g-C_3N_4-Fe_2O_3 nanocomposite

Material	PL Emission Peaks (nm)	PL Intensity / Features	Critical Remarks
Fe_2O_3	Broad emission ~650–750 nm	High intensity, indicating charge recombination	- Strong PL emission suggests significant electron–hole recombination. - Not ideal for photocatalytic applications without modification.
g-C_3N_4	Emission peaks ~450–500 nm	Moderate intensity, smaller peak width	- Lower PL intensity implies reduced charge recombination. - Shows good photocatalytic potential due to better charge carrier separation.
g-C_3N_4–Fe_2O_3	Emission peaks ~550–600 nm, redshifted	Reduced PL intensity, enhanced separation	- Reduced PL intensity indicates effective charge separation. - Improved photocatalytic activity due to reduced electron–hole recombination.

3.8 Nitrogen Adsorption-Desorption Isotherms (BET Surface Area Analysis)

Nitrogen Adsorption-Desorption Isotherms (BET Surface Area Analysis) provide key insights into the materials' surface area and pore structure**(Table 10).**Fe_2O_3 exhibits a moderate BET surface area (~45–65 m²/g) with mesoporous characteristics, which are suitable for catalysis but could be optimized for higher efficiency. g-C_3N_4 shows a higher surface area (~60–90 m²/g) and microporous structure, making it an excellent candidate for photocatalytic applications due to its ability to retain charge carriers[50]. The g–C_3N_4–Fe_2O_3 composite shows a significant increase in both surface area (~90–120 m²/g) and pore volume, which enhances its catalytic and photocatalytic performance, as the improved porosity allows for better diffusion of reactants and more active sites for reaction[51].

Table 10. BET surface and pore analysis of g-C_3N_4, Fe_2O_3, and g-C_3N_4-Fe_2O_3 nanocomposite

Material	BET Surface Area (m²/g)	Pore Volume (cm³/g)	Pore Size Distribution	Critical Remarks
Fe_2O_3	~45–65 m²/g	~0.1–0.2 cm³/g	Mesoporous (~2–50 nm)	- Moderate surface area with mesoporous structure. - Pore volume indicates potential for catalytic applications, but could be optimized for better efficiency.
g-C_3N_4	~60–90 m²/g	~0.2–0.3 cm³/g	Microporous (~1–2 nm)	- Relatively high surface area suitable for photocatalytic applications. - Micropores provide a good framework for charge carrier retention.
g-C_3N_4–Fe_2O_3	~90–120 m²/g	~0.3–0.4 cm³/g	Mixed (micro- and mesoporous)	- Increased surface area and pore volume after composite formation. - Enhanced catalytic and photocatalytic properties due to improved porosity.

3.9 Thermogravimetric Analysis (TGA)

Thermogravimetric Analysis (TGA) reveals essential information about the materials' thermal stability and decomposition behaviour **(Table 11).**Fe_2O_3 demonstrates excellent thermal stability with only a minor weight loss (~5–10%) occurring between 200–300°C due to the removal of adsorbed water, remaining stable up to 700°C[52]. g-C_3N_4, on the other hand, undergoes a significant weight loss (~20–30%) between 300–500°C, indicating decomposition of the organic framework, with stability up to 500°C. The g–C_3N_4–Fe_2O_3 composite shows a two-step weight loss, the first corresponding to water and surface group removal (200–300°C), and the second associated with the thermal decomposition of g-C_3N_4 (500–600°C). The composite's thermal stability is improved compared to pure g-C_3N_4, highlighting the interaction between the components[53].

Table 11. TGA of g-C_3N_4, Fe_2O_3, and g-C_3N_4-Fe_2O_3 nanocomposite

Material	Initial Weight Loss (°C)	Total Weight Loss (%)	Thermal Stability (°C)	Critical Remarks
Fe_2O_3	200–300°C	~5–10%	Stable up to	- Fe_2O_3 shows excellent thermal stability.

Material	Initial Weight Loss (°C)	Total Weight Loss (%)	Thermal Stability (°C)	Critical Remarks
			700°C	- Minor weight loss at lower temperatures due to surface adsorbed water.
g-C_3N_4	300–500°C	~20–30%	Stable up to 500°C	- Noticeable weight loss due to decomposition of organic material. - Thermal degradation occurs within a specific range, indicating moderate stability.
g-C_3N_4–Fe_2O_3	200–300°C and 500–600°C	~10–20%	Stable up to 600°C	- Composite shows a two-step weight loss. - First loss is attributed to water removal and surface groups, second to decomposition of g-C_3N_4.

3.10 Vibrating Sample Magnetometry (VSM)

Vibrating Sample Magnetometry (VSM) measurements reveal distinct magnetic behaviours in the materials**(Table 12).**Fe_2O_3 shows weak paramagnetic behaviour, with a saturation magnetisation of ~15–30 emu/g, making it suitable for magnetic separation in photocatalytic applications. g-C_3N_4 is non-magnetic, contributing no magnetic properties to the composite but offering a stable platform for Fe_2O_3 integration. The g–C_3N_4–Fe_2O_3 composite exhibits superparamagnetic behaviour, with a higher saturation magnetisation (~25–45 emu/g), indicating that the composite's magnetic response is significantly enhanced, which is beneficial for efficient separation and recycling after photocatalytic reactions[54].

Table 12. Magnetic measurement of g-C_3N_4, Fe_2O_3, and g-C_3N_4-Fe_2O_3 nanocomposite

Material	Magnetic Properties	Saturation Magnetization (emu/g)	Critical Remarks
Fe_2O_3	Paramagnetic behavior	~15–30 emu/g	- Exhibits weak magnetism, typical for Fe_2O_3. - Potential for magnetic separation in photocatalytic applications.
g-C_3N_4	Non-magnetic	0 emu/g	- g-C_3N_4 is inherently non-magnetic, providing a stable platform for composite formation. - No contribution to magnetic properties.
g-C_3N_4–Fe_2O_3	Superparamagnetic behaviour	~25–45 emu/g	- g-C_3N_4–Fe_2O_3 composite exhibits superparamagnetic properties. - Enhanced magnetic response facilitates easy separation after catalytic processes.

Mechanism of Photocatalytic Activity in g-C_3N_4-Fe_2O_3 Nanocomposites

The graphitic carbon nitride (g-C_3N_4) has garnered particular attention due to its unique combination of visible-light activity, suitable band structure, and chemical versatility, making it a highly promising candidate for forming efficient Fe_2O_3-based heterojunction photocatalysts.In photocatalytic degradation,mechanisms play a very significant role in improving the efficiency of composite materials. There are various types of

mechanisms studied in the literature for composite materials, viz. Type-II, Z-scheme, and S-scheme are discussed, along with their identification techniques and advantages.

Table 13: Photocatalytic Performance and Mechanisms of $Fe_2O_3/g\text{-}C_3N_4$ Composites

No.	Composite Material	Mechanism Type	Target Pollutant / Activity	Photocatalytic Performance	Reference
1	$Fe_2O_3/g\text{-}C_3N_4$	Z-scheme	Rhodamine B (RhB)	Rate constant 2.5 times higher than g-C_3N_4 alone under visible light	[55]
2	$Fe_2O_3/g\text{-}C_3N_4$	Z-scheme	H_2 generation	13-fold enhancement in H_2 evolution rate under visible light with Pt as co-catalyst	[56]
3	$Fe_2O_3/g\text{-}C_3N_4$	Type-II	Phenol	Achieved 94% degradation in visible light conditions	[57]
4	g-C_3N_4/α-Fe_2O_3/Co_3S_4	S-scheme	H_2 production	Hydrogen evolution rate of 191.41 μmol, ~30 times higher than Co_3S_4 alone	[58]

4.1 Type-II Heterojunction Mechanism

In the TypeII heterojunction mechanism of the g-C_3N_4–Fe_2O_3 composite,mainlyphotogenerated electrons(e^-) in the conduction band (CB) of g-C_3N_4 transfer to the CB of Fe_2O_3, while holes(h^+) from the valence band (VB) of Fe_2O_3 migrate to the VB of g-C_3N_4. This spatial separation promotes effective charge transfer and reduces recombination, enhancing hydroxyl radical (•OH) generation crucial for photo-Fenton activity (**Fig.3**). Unlike the Z-scheme, which retains strong redox potentials by recombining less energetic charge carriers, and the S-scheme that selectively directs high-energy charges while filtering low-energy ones, the Type II system sacrifices some redox power for better charge separation and stability[44].

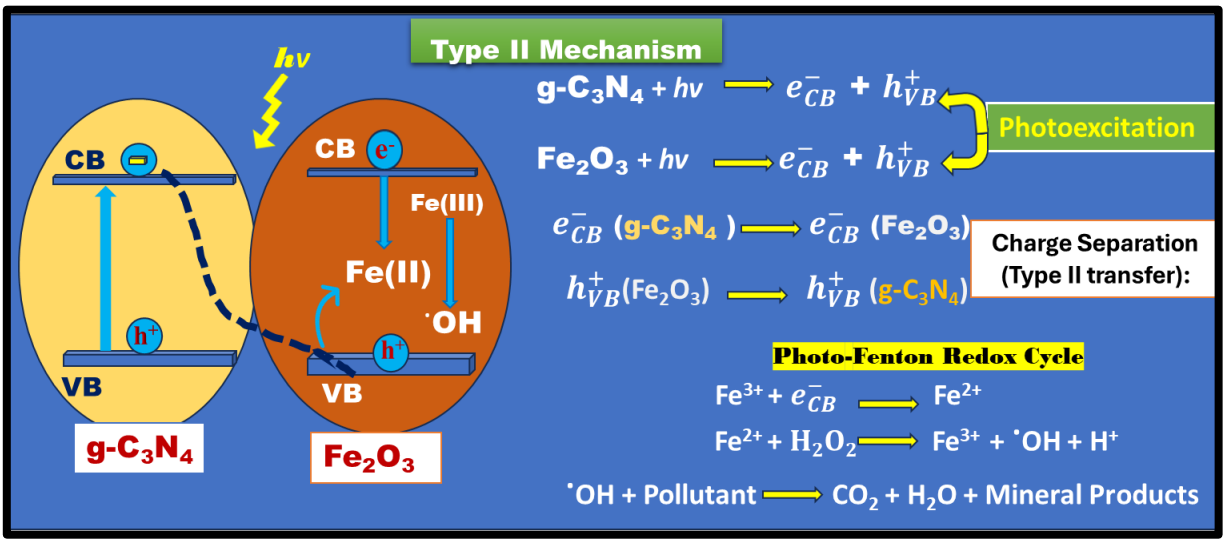

*Fig.3*Type II Photocatalytic Mechanism

g-C_3N_4 and Fe_2O_3 form a Type-II heterojunction in which the band alignment enables directional charge separation:

- Electrons from the g-C_3N_4 conduction band (CB, ~–1.1 eV) transfer to the Fe_2O_3 CB (+0.3 eV).
- Holes from the Fe_2O_3 valence band (VB, +2.6 eV) move to the g-C_3N_4 VB (+1.6 eV).

Redox limitations arise due to the energy positions of the bands:

- Electrons in the Fe_2O_3 CB (+0.3 eV) are insufficient to reduce O_2 to $\cdot O_2^-$ (–0.33 eV).
- Holes in the g-C_3N_4 VB (+1.6 eV) cannot oxidize OH^- to ·OH (+1.99 eV).

This limited redox potential hinders the formation of reactive oxygen species (ROS), essential for effective photocatalytic degradation.

Identification of the Type-II mechanism is supported by:

- UV-DRS and UPS measurements that confirm band alignment.
- Moderate photocurrent and high photoluminescence (PL), indicating charge recombination.
- Weak ESR signals for ·OH and $\cdot O_2^-$, indicating low ROS production.

4.2 Z-Scheme Heterojunction Mechanism

The Z-scheme mechanism allows recombination of low-energy carriers, preserving high-energy electrons and holes with strong redox ability. This mechanism is preferred in Fe_2O_3–g-C_3N_4 systems (**Fig.4**) [59].

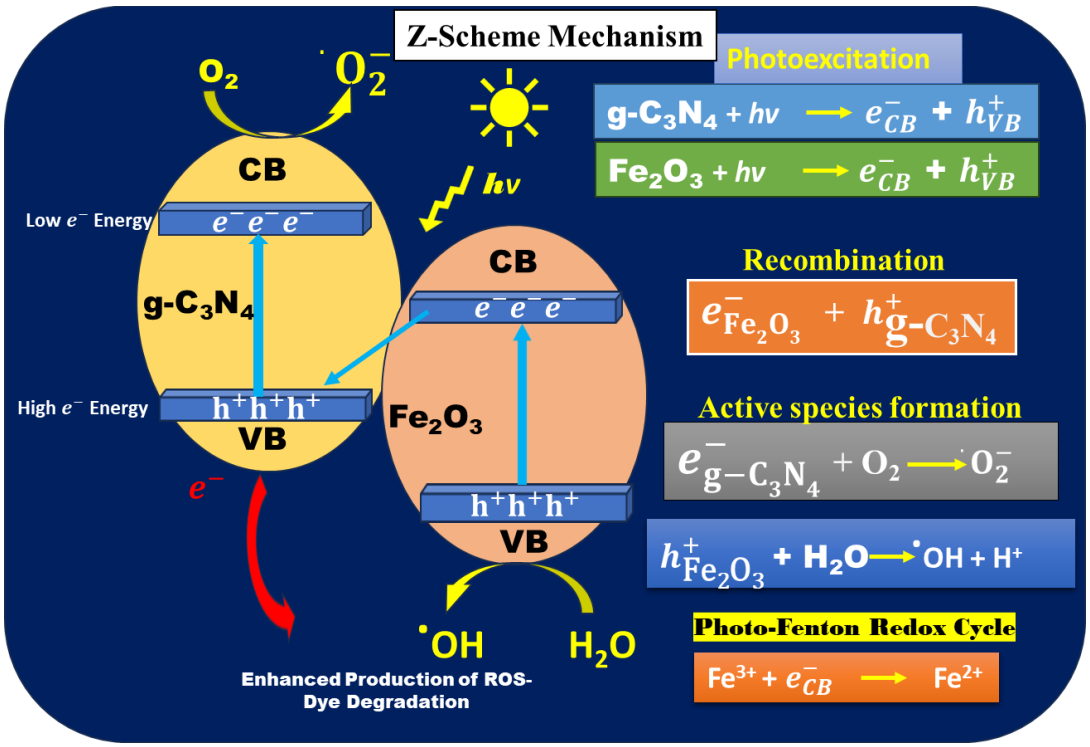

Fig.4. Z Scheme Photocatalytic Mechanism

Mechanism Details:

- e^- in Fe_2O_3 CB (+0.3 eV) recombines with h^+ in g-C_3N_4 VB (+1.6 eV)
- High-energy e^- in g-C_3N_4 CB (–1.1 eV) reduce $O_2 \rightarrow \cdot O_2^-$
- High-energy h^+ in Fe_2O_3 VB (+2.6 eV) oxidize $H_2O/OH^- \rightarrow$ ·OH
- Enhanced production of ROS → dye degradation

Advantages:

- Retains full redox potential
- Effective for the degradation of various dye pollutants

Identified by:

- Band edge analysis via XPS/UPS
- Strong signals of $\cdot O_2^-$ and ·OH via ESR spectroscopy
- Efficient charge carrier dynamics (low PL, high photocurrent)

4.3 S-Scheme Heterojunction Mechanism

The S-scheme (step-scheme) is a new-generation heterojunction model that retains the high redox ability like Z-scheme but incorporates built-in electric field (IEF) and band bending to enhance charge carrier separation further (**Fig.5**) [60].

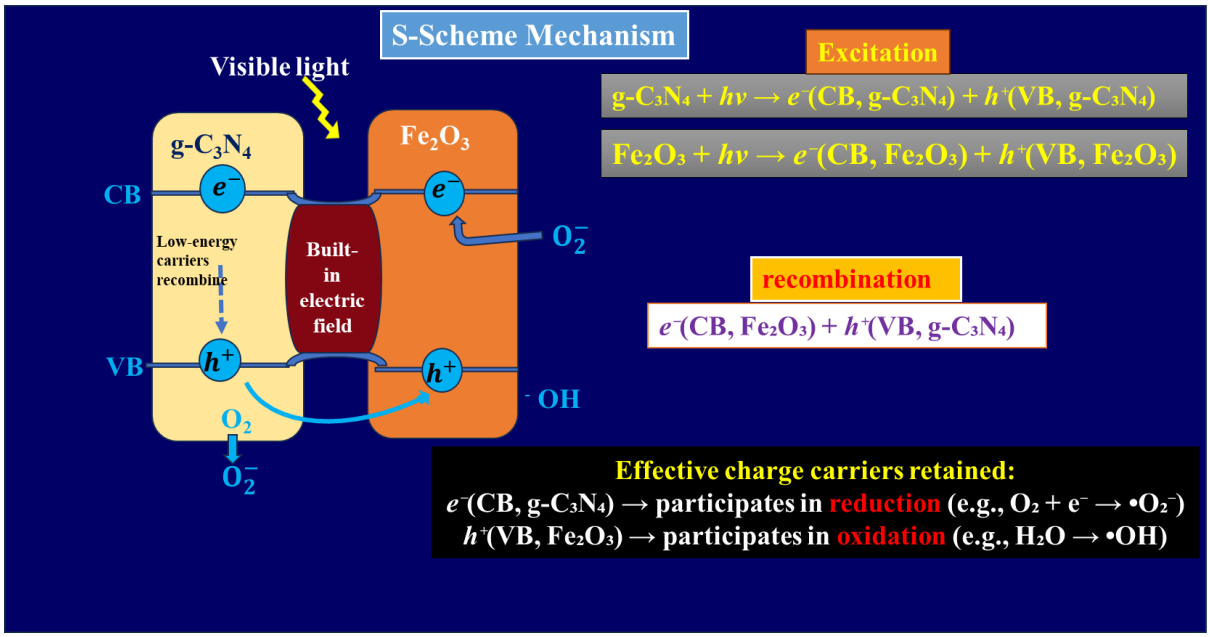

Fig.5

Mechanism Details:

- Upon contact, band bending and IEF form at the interface
- Low-energy carriers recombine at the interface
- High-energy e^- from CB of g-C_3N_4 and h^+ from VB of Fe_2O_3 are spatially separated
- Facilitates formation of $\cdot O_2^-$ and •OH radicals, key for dye degradation

Advantages:

- Strong internal field promotes ultrafast carrier migration
- Effective under visible light due to narrow bandgap and synergistic behavior

Identified by:

- Mott–Schottky plots (to determine flat band positions)
- Time-resolved PL spectroscopy
- XPS depth profiling (evidence of Fermi level alignment)
- Transient photocurrent, lower charge transfer resistance in EIS

Table 14 summarizes the comparison of charge transfer mechanisms and photocatalytic efficiencies among Type II, Z-scheme, and S-scheme heterojunctions.

Table 14. of Mechanisms, ROS, and Dyes Degraded.

Feature	Type II	Z-Scheme	S-Scheme
Charge Flow Direction	CB (g-C_3N_4) → CB (Fe_2O_3), VB (Fe_2O_3) → VB (g-C_3N_4)	CB (Fe_2O_3) → VB (g-C_3N_4) (recombination)	Similar to Z-scheme but with a **built-in electric field** aiding separation
Redox Potential Retention	**Reduced** (lower redox ability)	**Retained** (strong oxidation/reduction retained)	**Retained** with added driving force via internal field

Feature	Type II	Z-Scheme	S-Scheme
Main Advantage	Efficient charge separation	High redox potential maintained	Strong charge separation + high redox ability
Suitable for	Mild reactions (e.g., dye degradation via Fenton)	Reactions needing strong redox power	High-efficiency photocatalysis with enhanced selectivity

5Fe_2O_3–g-C_3N_4 Nanocomposites for Sustainable Environmental Application

Iron oxide graphitic carbon nitride nanocomposites have emerged as auspicious materials for various environmental remediation applications, particularly for degrading organic pollutants from wastewater. The synergistic integration of iron oxide (Fe_2O_3), known for its strong redox properties, with graphitic carbon nitride (g-C_3N_4), valued for its high surface area, visible light response, and chemical stability, results in enhanced photocatalytic performance. These nanocomposites efficiently degrade persistent contaminants such as dyes, pharmaceutical residues, and pesticides under visible or solar irradiation, often achieving rapid degradation rates due to improved charge carrier separation and extended light absorption capacity[61]. Additionally, they are used for hydrogen production via water splitting and CO_2 reduction, contributing to clean energy solutions. Notably, the nanocomposites achieve substantial dye degradation in markedly shorter reaction timesunder UV-visible or sunlight. This confirms the enhanced interfacial charge transfer and wider light absorption achieved through composite formation (Table 15).Their reusability, cost-effectiveness, and ability to function under solar irradiation make them attractive for sustainable environmental remediation.

Table 15. Photocatalytic degradation of organic dyes using Fe_2O_3, g-C_3N_4, and their composites

Pollutant (Dye)	Material	Light Source	Photocatalytic Efficiency	Reaction Time	Performance of Composite vs. Individual	Reference
Methyl Orange (MO)	Fe_2O_3	Sunlight	~60%	90 min	–	[62]
	g-C_3N_4	Sunlight	~65%	120 min	–	
	Fe_2O_3/g-C_3N_4	Sunlight	**96.5%**	60 min	Significant enhancement	
Methylene Blue (MB)	Fe_2O_3	Visible light	~53%	120 min	–	[63]
	g-C_3N_4	Visible light	~38%	120 min	–	
	Fe_2O_3/g-C_3N_4	Visible light	**89%**	120 min	Strong enhancement	
Rhodamine B (RhB)	Fe_2O_3	Sun light	~58%	150 min	–	[64]
	g-C_3N_4	Sun light	~64%	150 min	–	
	Fe_2O_3/g-C_3N_4	Sun light	**93%**	150 min	Excellent improvement	
Methyl Orange (MO)	Fe_2O_3	Visible light	39.33%	60 min	–	[32]

Pollutant (Dye)	Material	Light Source	Photocatalytic Efficiency	Reaction Time	Performance of Composite vs. Individual	Reference
	g-C_3N_4	Visible light	45.33%	60 min	–	
	Fe_2O_3/g-C_3N_4	Visible light	**97.66%**	60 min	Superior activity	
Orange II	α-Fe_2O_3	Visible light	~40%	150 min	–	[65]
	g-C_3N_4/α-Fe_2O_3	Visible light	~60%	150 min	–	
	g-C_3N_4/α-Fe_2O_3/Fe_3O_4	Visible light	**79%**	150 min	Significant enhancement	
Crystal Violet (CV)	Fe_2O_3	Sun Light	72%	150 min	–	[66]
	g-C_3N_4	Sun Light	85%	150 min	–	
	g-C_3N_4/Fe_2O_3	Sun Light	**95%**	1500 min	Significant enhancement	

5.1 Factors Influencing Photocatalytic Performance

Several key parameters, including the Fe_2O_3:g-C_3N_4 ratio, surface area, doping, and morphology, influence the efficiency of Fe_2O_3/g-C_3N_4 nanocomposites. Optimal ratios improve interface contact and charge transfer, while porous structures enhance dye adsorption. Metal or non-metal doping suppresses recombination and extends visible-light absorption. Environmental factors such as pH, light source, and dye type also impact performance. Tailoring these factors can significantly boost photocatalytic outcomes, though long-term stability still needs improvement. These key factors, which are critical for enhancing real-world efficacy, are summarized in Table 16.

Table 16. Influencing factors of dye degradation performance

Factor	Influence on Performance
Composite Ratio (Fe_2O_3/g-C_3N_4)	Affects interface contact, electron transfer, and light absorption. Too much Fe_2O_3 may shield light; too little reduces.
Morphology and Surface Area	Higher surface area = more active sites. Porous/hollow structures improve dye adsorption and light scattering.
Doping with Metal/Non-metals	Enhances conductivity, suppresses recombination, and tunes bandgap.
Co-catalysts	Noble metals (Ag, Pt) or graphene can act as electron sinks, enhancing charge separation.
pH of Solution	Affects surface charge, dye ionization, and ROS generation. Optimal pH is often dye-specific.
Light Source	g-C_3N_4 is visible-light active; Fe_2O_3 absorbs in both regions. The composite shows good

Factor	Influence on Performance
(UV/Visible)	performance under sunlight.
Reusability and Stability	Reusability isessential for practical use. Magnetic Fe_2O_3 allows easy separation; stability ensures long-term use.

5.2 Comparative Analysis with Other Photocatalysts

Fe_2O_3/g-C_3N_4 composites outperform many conventional photocatalysts like TiO_2 and ZnO due to their broader light absorption and efficient charge separation via Z-/S-scheme mechanisms. While TiO_2 and ZnO are UV-active, the composite works efficiently under visible and solar light, often achieving >90% dye degradation. Its magnetic recoverability adds practical value. Moreover, green synthesis routes make it cost-effective and sustainable, although real wastewater conditions and reusability under field conditions need further evaluation.

Photocatalyst	Light Absorption	Charge Separation Efficiency	Photodegradation Efficiency (e.g., Methyl Orange)	Reusability	Cost & Sustainability	Limitations
TiO_2 (P25)	UV-active only (λ < 380 nm)	Moderate	~60–70% in 120 min (UV)	Moderate (5 cycles)	Cheap, abundant	Limited visible light use
ZnO	UV-active	Fast recombination	~65–75% in 120 min (UV)	Moderate	Simple synthesis	Photo corrosion under light
g-C_3N_4	Visible-light active (λ ~450 nm)	Low (fast recombination)	~50–60% in 120 min (visible)	Good	Green, metal-free	Needs heterojunctions to improve
Fe_2O_3 alone	Visible (λ ~550 nm)	Poor (recombination)	~40–55% in 120 min	Limited	Earth-abundant	Low surface area, slow kinetics
Fe_2O_3/g-C_3N_4	Wide range (UV + visible)	High (via Z-/S-scheme)	>90% in 90–120 min (visible or sunlight)	High (easy recovery via magnetism)	Eco-friendly (green synthesis possible)	Slightly lower activity under weak indoor light

Conclusion and Future Outlook

Iron oxide (Fe_2O_3)–graphitic carbon nitride (g-C_3N_4) nanocomposites represent a compelling class of visible-light-responsive photocatalysts that synergistically merge the magnetic, redox-active nature of Fe_2O_3 with the narrow bandgap and high stability of g-C_3N_4. Their integration forms effective Z-scheme or S-scheme heterojunctions, enhancing charge carrier separation and extended light absorption, attributes vital for efficiently degrading toxic organic dyes and pollutants.

This review has illustrated that the synthetic approaches, characterization techniques, mechanisms, and environmental applications of Fe_2O_3-g-C_3N_4 nanocomposites are closely aligned with green chemistry

principles for sustainable nanomaterial production.These materials have demonstrated more than 90% degradation of various dyes such as methyl orange, methylene blue, rhodamine B, Orange II, crystal violet, and congo red under UV-visibleand sunlight, facilitated by advanced charge-transfer mechanisms and surface reactivity.However, a critical scientific analysis reveals notable limitations and research gaps:Incomplete mechanistic validation is often based solely on photoluminescence or UV-DRS without the support of TRPL, ESR, XPS, or scavenger-trapping experiments.Poor reproducibility of green-synthesized composites due to non-uniform precursor sources.Over multiple cycles, there is limited data on long-term photocatalyst stability, iron leaching, and reusability.Scarcity of real-effluent degradation studies, which are crucial for practical wastewater treatment.Inadequate monitoring of toxic degradation intermediates poses risks despite high decolorization efficiency.

To bridge these gaps, future research must focus on:

- Mechanistic studies using multi-spectral characterizations (e.g., TRPL, EIS, ESR, XPS) to gain deeper insights into charge transfer and active site dynamics.
- Standardized synthesis protocols for reproducible and scalable nanocomposite development, critical for real-world applications.
- Testing in real industrial wastewater and multi-component pollutant systems (dyes, antibiotics, heavy metals) to assess practical performance.
- Integration of ternary or doped systems (e.g., Fe_2O_3/g-C_3N_4/Ag) to boost photocatalytic and biological efficiency.
- Device-level implementation, such as coated membranes, 3D sponges, and magnetically retrievable platforms, to facilitate field applications.
- Expanding composite applications into energy storage devices and electrochemical sensing enhances multifunctionality.

Based on the comprehensive analysis of existing literature, future studies should prioritize scalable green synthesis methods, advanced mechanistic investigations through in-depth characterization, and expansion of application domains beyond dye degradation to include real wastewater treatment, hydrogen production, CO_2 reduction, and a stronger emphasis on energy storage devicesaligning with global sustainability goals.

Acknowledgments

Mr. B.T. Shinde would like to extend our sincere appreciation to the Research Centre, Department of Chemistry, A.S.P. College (Autonomous), Devrukh, and S.K.S.V. College, Lanja, Ratnagiri, Maharashtra, India, for their valuable assistance and provision of essential resources for the successful execution of this research work.

Author Contributions:

Babasaheb T. Shinde: Conceptualization, literature review, writingoriginal draft preparation, and data analysis.Dr. Hemant V. Chavan: Supervision, guidance throughout the research and writing process, critical revision of the manuscript, and final approval of the version to be submitted.

Conflicts of Interest:

The authors declare that there is no conflict of interest regarding the publication of this article.

REFERENCES

[1]. F. Yang and P. Boulet, “DFT Investigation of a Direct Z-Scheme Photocatalyst for Overall Water Splitting : Janus Ga 2 SSe / Bi 2 O 3 Van Der Waals Heterojunction,” 2025.

[2]. H. W. Ahmad, H. A. Bibi, M. Chandrasekaran, S. Ahmad, and G. L. Kyriakopoulos, "Sustainable Wastewater Treatment Strategies in Effective Abatement of Emerging Pollutants," 2024.

[3]. S. B. Babar et al., "An efficient fabrication of ZnO–carbon nanocomposites with enhanced photocatalytic activity and superior photostability," J. Mater. Sci. Mater. Electron., vol. 30, no. 2, pp. 1133–1147, 2019, doi: 10.1007/s10854-018-0382-5.

[4]. M. A. Hassaan, M. A. El, and N. Marwa, Principles of Photocatalysts and Their Different Applications : A Review, vol. 381, no. 6. Springer International Publishing, 2023. doi: 10.1007/s41061-023-00444-7.

[5]. S. P. Keerthana et al., "A strategy to enhance the photocatalytic efficiency of α-Fe2O3," Chemosphere, vol. 270, p. 129498, 2021, doi: 10.1016/j.chemosphere.2020.129498.

[6]. Y. L. Pang, S. Lim, and H. C. Ong, "Research progress on iron oxide-based magnetic materials: Synthesis techniques and photocatalytic applicationsAuthor ' s Accepted Manuscript applications," Ceram. Int., vol. 15, no. August, pp. 01670–3, 2015, doi: 10.1016/j.ceramint.2015.08.144.

[7]. N. Farooq, M. Imran, A. Mahmood, M. Ahmad, A. Shanableh, and S. Anjum, "Fe 2 O 3 / g-C 3 N 4 / CNTs based nanocomposites incorporated with neodymium and samarium nanoparticles for efficient photocatalytic vitiation of organic pollutants," vol. 259, pp. 71–81, 2022, doi: 10.5004/dwt.2022.28444.

[8]. S. S. Yi, J. M. Yan, and Q. Jiang, "Carbon quantum dot sensitized integrated Fe2O3@g-C3N4 core-shell nanoarray photoanode towards highly efficient water oxidation," J. Mater. Chem. A, vol. 6, no. 21, pp. 9839–9845, 2018, doi: 10.1039/c8ta01908h.

[9]. W. J. Ong, L. L. Tan, Y. H. Ng, S. T. Yong, and S. P. Chai, "Graphitic Carbon Nitride (g-C3N4)-Based Photocatalysts for Artificial Photosynthesis and Environmental Remediation: Are We a Step Closer to Achieving Sustainability?," Chemical Reviews, vol. 116, no. 12. pp. 7159–7329, 2016. doi: 10.1021/acs.chemrev.6b00075.

[10]. Y. Wang, X. Wang, and M. Antonietti, "Polymeric graphitic carbon nitride as a heterogeneous organocatalyst: From photochemistry to multipurpose catalysis to sustainable chemistry," Angew. Chemie - Int. Ed., vol. 51, no. 1, pp. 68–89, 2012, doi: 10.1002/anie.201101182.

[11]. K. S. Novoselov et al, "Electric Field Effect in Atomically Thin Carbon Films," vol. 306, no. 5696, pp. 666–669, 2016.

[12]. A. K. G. A. K. S. NOVOSELOV, "The rise of graphene," Nat. Mater, vol. 6, pp. 183–191, 2007, doi: 10.1007/978-3-319-70329-9.

[13]. S. Pei and H. M. Cheng, "The reduction of graphene oxide," Carbon N. Y., vol. 50, no. 9, pp. 3210–3228, 2012, doi: 10.1016/j.carbon.2011.11.010.

[14]. D. R. Dreyer, S. Park, C. W. Bielawski, and R. S. Ruoff, "The chemistry of graphene oxide," Chem. Soc. Rev., vol. 39, no. 1, pp. 228–240, 2010, doi: 10.1039/b917103g.

[15]. G. Eda and M. Chhowalla, "Chemically derived graphene oxide: Towards large-area thin-film electronics and optoelectronics," Adv. Mater., vol. 22, no. 22, pp. 2392–2415, 2010, doi: 10.1002/adma.200903689.

[16]. D. Konios, M. M. Stylianakis, E. Stratakis, and E. Kymakis, "Dispersion behaviour of graphene oxide and reduced graphene oxide," J. Colloid Interface Sci., vol. 430, pp. 108–112, 2014, doi: 10.1016/j.jcis.2014.05.033.

[17]. X. Pan, M. Q. Yang, X. Fu, N. Zhang, and Y. J. Xu, "Defective TiO2 with oxygen vacancies: Synthesis, properties and photocatalytic applications," Nanoscale, vol. 5, no. 9, pp. 3601–3614, 2013, doi: 10.1039/c3nr00476g.

[18]. Y. Song, P. C. D. Mendes, and S. M. Kozlov, "Tunable properties and composition of ZnO films supported on metal surfaces," J. Mater. Chem. A, vol. 11, no. 25, pp. 13665–13676, 2023, doi: 10.1039/d3ta01940c.

[19]. L. Yang et al., “Fabrication of semiconductor ZnO nanostructures for versatile SERS application,” Nanomaterials, vol. 7, no. 11, 2017, doi: 10.3390/nano7110398.

[20]. X. Zhang, W. Lu, G. Zhou, and Q. Li, “Understanding the Mechanical and Conductive Properties of Carbon Nanotube Fibers for Smart Electronics,” Adv. Mater., vol. 32, no. 5, pp. 1–21, 2020, doi: 10.1002/adma.201902028.

[21]. P. Udomkun, T. Boonupara, S. M. Smith, and P. Kajitvichyanukul, “Green Ag/AgCl as an Effective Plasmonic Photocatalyst for Degradation and Mineralization of Methylthioninium Chloride,” Separations, vol. 9, no. 8, pp. 1–17, 2022, doi: 10.3390/separations9080191.

[22]. F. R. Oliveira, A. K. Patel, D. P. Jaisi, S. Adhikari, H. Lu, and S. K. Khanal, “Environmental application of biochar: Current status and perspectives,” Bioresour. Technol., vol. 246, pp. 110–122, 2017, doi: 10.1016/j.biortech.2017.08.122.

[23]. A. Sánchez, “Editorial: Innovative uses of biochar in environmental applications,” Front. Chem. Eng., vol. 6, no. September, pp. 1–2, 2024, doi: 10.3389/fceng.2024.1474937.

[24]. L. Zhou, L. Wang, J. Zhang, J. Lei, and Y. Liu, “Well-Dispersed Fe2O3Nanoparticles on g-C3N4for Efficient and Stable Photo-Fenton Photocatalysis under Visible-Light Irradiation,” Eur. J. Inorg. Chem., vol. 2016, no. 34, pp. 5387–5392, 2016, doi: 10.1002/ejic.201600959.

[25]. P. Dhull, R. K. Lohchab, M. Kumari, K. Singh, and A. K. Bhankhar, “A Facile Method for Synthesis of α-Fe 2 O 3 Nanoparticles and Assessment of Their Characterization,” Nat. Environ. Pollut. Technol., vol. 23, pp. 321–330, 2024.

[26]. S. Sundar and G. Venkatachalam, “Nanostructures for the Selective and Sensitive Determination of Uric Acid and Dopamine,” Catalysts, vol. 8, no. 11, p. 512, 2018, doi: 10.3390/catal8110512.

[27]. J. Ma, J. Lian, X. Duan, X. Liu, and W. Zheng, “r -Fe 2 O 3 : Hydrothermal Synthesis , Magnetic and Electrochemical Properties,” pp. 10671–10676, 2010.

[28]. M. Diab and T. Mokari, “Thermal Decomposition Approach for the Formation of α - Fe 2 O 3 Mesoporous Photoanodes and an α - Fe 2 O 3 /CoO Hybrid Structure for Enhanced Water Oxidation,” pubs.acs.org/IC Therm., vol. 53, p. 2304–2309, 2014.

[29]. P. C. Implementation, “Synthesis and Characterization of α -Fe 2 O 3 Nanoparticles by Microemulsion Method Gamze BOZKURT 1* 1,” J. Sci. Technol., vol. 13, no. 2, pp. 890–897, 2020, doi: 10.18185/erzifbed.742160.

[30]. V. C. Karade et al., “Heliyon A green approach for the synthesis of α -Fe 2 O 3 nanoparticles from Gardenia resinifera plant and it ’ s In vitro hyperthermia application,” Heliyon, vol. 5, no. February, p. e02044, 2019, doi: 10.1016/j.heliyon.2019.e02044.

[31]. H. J. Fatih, M. Ashengroph, and A. Sharifi, “potent antibacterial , anti-biofilm and anti- virulence agent against pathogenic bacteria,” BMC Microbiol., vol. 24, no. 535, pp. 1–13, 2024.

[32]. B. T. Shinde, S. B. Babar, U. V. Shembade, A. V. Moholkar, and H. V. Chavan, “Efficient chemical synthesis of g–C3N4–Fe2O3 nanocomposites as a photocatalyst for superior photocatalytic degradation,” Res. Chem. Intermed., vol. 51, no. 3, pp. 1511–1535, 2025, doi: 10.1007/s11164-025-05514-7.

[33]. Q. Tao, J. Bi, X. Huang, R. Wei, T. Wang, and Y. Zhou, “Chemosphere Fabrication , application , optimization and working mechanism of Fe 2 O 3 and its composites for contaminants elimination from wastewater,” Chemosphere, vol. 263, p. 127889, 2021, doi: 10.1016/j.chemosphere.2020.127889.

[34]. B. Chen, S. Hatamie, P. Garu, P. Heravi, J. Chen, and B. Liu, “Synthesis of iron-oxide magnetic nanoparticles coated with dextran of varied molecular mass using a facile ball-milling method,” Micro Nano Lett., vol. 15, no. 10, pp. 645–650, 2020, doi: 10.1049/mnl.2019.0811.

[35]. S. Babar et al., "Evolution of Waste Iron Rust into Magnetically Separable g-C3N4-Fe2O3 Photocatalyst: An Efficient and Economical Waste Management Approach," ACS Appl. Nano Mater., vol. 1, no. 9, pp. 4682–4694, Sep. 2018, doi: 10.1021/acsanm.8b00936.

[36]. S. B. Shinde, O. S. Nille, A. H. Gore, N. B. Birajdar, G. B. Kolekar, and P. V Anbhule, "Valorization of Waste Tungsten Filament into mpg - C 3 N 4 – WO 3 Photocatalyst : A Sustainable e - Waste Management and Wastewater Treatment," Langmuir, vol. 38, no. 44, p. 13543–13557, 2022, doi: 10.1021/acs.langmuir.2c02171.

[37]. B. Palanivel et al., "Green synthesis of Fe2O3 deposited g-C3N4: Addition of rGO promoted Z-scheme ternary heterojunction for efficient photocatalytic degradation and H2 evolution reaction," Mater. Res. Bull., vol. 162, no. January, p. 112177, 2023, doi: 10.1016/j.materresbull.2023.112177.

[38]. S. Vasantharaj, N. Sripriya, M. Shanmugavel, E. Manikandan, A. Gnanamani, and P. Senthilkumar, "Surface active gold nanoparticles biosynthesis by new approach for bionanocatalytic activity," J. Photochem. Photobiol. B Biol., vol. 179, pp. 119–125, 2018, doi: 10.1016/j.jphotobiol.2018.01.007.

[39]. L. Luo, A. Zhang, M. J. Janik, C. Song, and X. Guo, "Mesoporous graphitic carbon nitride functionalized iron oxides for promoting phenol oxidation activity," RSC Adv., vol. 6, no. 94, pp. 91960–91967, 2016, doi: 10.1039/c6ra19455a.

[40]. M. Ashraf et al., "Heliyon Fabrication and characterization of novel , cost-effective graphitic carbon nitride / Fe coated textile nanocomposites for effective degradation of dyes and biohazards," Heliyon, vol. 9, no. 10, p. e20822, 2023, doi: 10.1016/j.heliyon.2023.e20822.

[41]. K. C. Christoforidis et al., "Synthesis and photocatalytic application of visible-light active ˇ -Fe 2 O 3 / g-C 3 N 4 hybrid nanocomposites".

[42]. S. Al, S. Thangavel, Y. Kim, and R. Selvaraj, "Enhanced photocatalytic activity of a -Fe 2 O 3 / g-C 3 N 4 composite materials for degradation of toluene in aqueous solution under visible light irradiation," vol. 254, pp. 94–103, 2022, doi: 10.5004/dwt.2022.28350.

[43]. D. Mhamane, H. K. Kim, V. Aravindan, K. C. Roh, M. Srinivasan, and K. B. Kim, "Rusted iron wire waste into high performance anode (α-Fe2O3) for Li-ion batteries: An efficient waste management approach," Green Chem., vol. 18, no. 5, pp. 1395–1404, Mar. 2016, doi: 10.1039/c5gc01747e.

[44]. F. Ge, X. Li, M. Wu, H. Ding, and X. Li, "RSC Advances PAPER A type II heterojunction a -Fe 2 O 3 / g-C 3 N 4 for the," RSC Adv., vol. 12, pp. 8300–8309, 2022, doi: 10.1039/D1RA09282K.

[45]. X. Hu, J. C. Yu, J. Gong, Q. Li, and G. Li, "α-Fe2O3 nanorings prepared by a microwave-assisted hydrothermal process and their sensing properties," Adv. Mater., vol. 19, no. 17, pp. 2324–2329, Sep. 2007, doi: 10.1002/adma.200602176.

[46]. V. Gaikwad, U. Kumar, F. Pahlevani, A. Piadasa, and V. Sahajwalla, "Thermal Transformation of Waste Toner Powder into a Value-Added Ferrous Resource," ACS Sustain. Chem. Eng., vol. 5, no. 12, pp. 11543–11550, 2017, doi: 10.1021/acssuschemeng.7b02875.

[47]. N. Farooq et al., "A comparative study of cerium- and ytterbium-based GO/g-C3N4/Fe2O3 composites for electrochemical and photocatalytic applications," Appl. Sci., vol. 11, no. 19, 2021, doi: 10.3390/app11199000.

[48]. N. X. D. Linh et al., "Facile Fabrication of α-Fe2O3/g-C3N4 Z Scheme Heterojunction for Novel Degradation of Residual Tetracycline," Top. Catal., vol. 66, no. 1–4, pp. 139–148, Jan. 2023, doi: 10.1007/s11244-022-01751-x.

[49]. A. Kheradmand, A. Wainwright, L. Wang, and Y. Jiang, "Anchoring Iron Oxides on Carbon Nitride Nanotubes for Improved Photocatalytic Hydrogen Production," Energy & Fuels, vol. 35, no. 1, pp. 868–876, 2021, doi: 10.1021/acs.energyfuels.0c03901.

[50]. D. R. Paul, S. Gautam, P. Panchal, S. P. Nehra, P. Choudhary, and A. Sharma, "ZnO-Modi fi ed g - C 3 N 4 : A Potential Photocatalyst for Environmental Application," 2020, doi: 10.1021/acsomega.9b02688.

[51]. R. Khurram, Z. U. Nisa, A. Javed, Z. Wang, and M. A. Hussien, "Synthesis and Characterization of an α -Fe 2 O 3 -Decorated g-C 3 N 4 Heterostructure for the Photocatalytic Removal of MO," 2022.

[52]. E. C. Spencer, N. L. Ross, R. E. Olsen, B. Huang, I. Alexander, and B. F. Woodfield, "Thermodynamic Properties of α -Fe 2 O 3 and Fe 3 O 4 Nanoparticles," pp. 1–19, 2008.

[53]. S. Babar et al., "An innovative transformation of waste toner powder into magnetic g-C3N4-Fe2O3 photocatalyst: Sustainable e-waste management," J. Environ. Chem. Eng., vol. 7, no. 2, Apr. 2019, doi: 10.1016/j.jece.2019.103041.

[54]. G. I. Tovar, S. Briceño, J. Suarez, S. Flores, and G. González, "Biogenic synthesis of iron oxide nanoparticles using Moringa oleifera and chitosan and its evaluation on corn germination," Environ. Nanotechnology, Monit. Manag., vol. 14, no. June, p. 100350, 2020, doi: 10.1016/j.enmm.2020.100350.

[55]. J. Hu, Shaozheng and Jin, Ruirui and Lu, Guang and Liu, Dan and Gui, "RSC Advances," RSC Adv, vol. 4, no. 47, pp. 24863–24869, 2014, doi: 10.1039/c4ra03290j.

[56]. Q. Xu, B. Zhu, C. Jiang, B. Cheng, and J. Yu, "Constructing 2D/2D Fe2O3/g-C3N4 Direct Z-Scheme Photocatalysts with Enhanced H2 Generation Performance," Sol. RRL, vol. 2, no. 3, pp. 1–10, 2018, doi: 10.1002/solr.201800006.

[57]. Y. Zhang, J. Wan, C. Zhang, and X. Cao, "MoS2 and Fe2O3 co-modify g-C3N4 to improve the performance of photocatalytic hydrogen production," Sci. Rep., vol. 12, no. 1, pp. 1–12, 2022, doi: 10.1038/s41598-022-07126-2.

[58]. T. Yan, H. Liu, and Z. Jin, "G-C3N4/α-Fe2O3Supported Zero-Dimensional Co3S4Nanoparticles Form S-Scheme Heterojunction Photocatalyst for Efficient Hydrogen Production," Energy and Fuels, vol. 35, no. 1, pp. 856–867, 2021, doi: 10.1021/acs.energyfuels.0c03351.

[59]. Y. pei Li et al., "Z-scheme electronic transfer of quantum-sized A-Fe2O3 modified g-C3N4 hybrids for enhanced photocatalytic hydrogen production," Int. J. Hydrogen Energy, vol. 42, no. 47, pp. 28327–28336, 2017, doi: 10.1016/j.ijhydene.2017.09.137.

[60]. H. Lv et al., "Multishelled hollow CaTiO3 cubes decorated with Co0.2Cd0.8S nanoparticles for efficient photocatalytic H2 evolution via S-scheme charge transfer," Sep. Purif. Technol., vol. 345, p. 127429, Oct. 2024, doi: 10.1016/J.SEPPUR.2024.127429.

[61]. M. A. Ahmed and A. A. Mohamed, "Recent progress in semiconductor/graphene photocatalysts: synthesis, photocatalytic applications, and challenges," RSC Adv., vol. 13, no. 1, pp. 421–439, 2022, doi: 10.1039/d2ra07225d.

[62]. S. Babar et al., "Evolution of Waste Iron Rust into Magnetically Separable g-C3N4-Fe2O3 Photocatalyst: An Efficient and Economical Waste Management Approach," ACS Appl. Nano Mater., vol. 1, no. 9, pp. 4682–4694, 2018, doi: 10.1021/acsanm.8b00936.

[63]. A. Ali et al., "g-C3N4/Fe3O4 composites synthesized via solid-state reaction and photocatalytic activity evaluation of methyl blue degradation under visible light irradiation," Front. Mater., vol. 10, no. May, pp. 1–11, 2023, doi: 10.3389/fmats.2023.1180646.

[64]. S. Kumaravel et al., "Rational construction of MOF derived α-Fe2O3/g-C3N4 composite for effective photocatalytic degradation of organic pollutants and electrocatalytic oxygen evolution reaction,"

Spectrochim. Acta - Part A Mol. Biomol. Spectrosc., vol. 310, no. November 2023, p. 123972, 2024, doi: 10.1016/j.saa.2024.123972.

[65]. Z. Wang et al., "Novel magnetic g-C3N4/α-Fe2O3/Fe3O4 composite for the very effective visible-light-fenton degradation of Orange II," RSC Adv., vol. 8, no. 10, pp. 5180–5188, 2018, doi: 10.1039/c7ra13291c.

[66]. T. Wang et al., "Facile one-step hydrothermal synthesis of α-Fe2O3/g-C3N4 composites for the synergistic adsorption and photodegradation of dyes," RSC Adv., vol. 9, pp. 29109–29119, 2019, doi: 10.1039/c9ra05100g.